Processing and improvements in dynamic quantitative phase microscope

Katherine Creath[1-3*] and Goldie Goldstein[1,2]
[1]4D Technology Corporation, Tucson AZ 85706,
[2]College of Optical Sciences, The University of Arizona, Tucson, AZ USA 85721 and,
[3]Optineering, Tucson, AZ USA 85719

ABSTRACT

This paper describes recent research and development related to data processing and imaging performance for a dynamic quantitative phase imaging microscope. This microscope provides instantaneous measurements of dynamic motions within and among live cells without labels or contrast agents. It utilizes a pixelated wire grid polarizer mask in front of the camera sensor that enables simultaneous measurement of multiple interference patterns. Optical path difference (OPD) and optical thickness (OT) data are obtained from phase images. Simulated DIC (gradient) and simulated dark field (gradient magnitude) images can be directly obtained from the phase enabling simultaneous capture of brightfield, phase contrast, quantitative phase, DIC and dark field. The OT is further processed to remove background shapes, and enhance topography. This paper presents a number of different processing routines to remove background surface shape enabling quantification of changes in cell position and volume over time. Data from a number of different moving biological organisms and cell cultures are presented.

Keywords: phase imaging, interference microscopy, polarization interferometry, cellular imaging, cell dynamics, optical thickness measurement, label-free imaging, 4D microscopy, quantitative phase microscopy

1. INTRODUCTION

Measurement of cellular dynamics and changes in cellular properties over time is important for understanding cellular physiology and function (see, for example, [1-3]). Most microscopes providing topographic information or quantitative phase require some sort of scanning and/or vibration isolation systems. Valuable information can be obtained when quantitative phase can be measured in a snapshot without the need for vibration isolation systems. Phase images can reveal features and quantitative data that are not available through other types of imaging.

Phase imaging techniques quantify optical thickness (OT) variations due to small variations in refractive index relating to variations in density of different structures and materials within cells and tissues. Very small refractive index variations can manifest as large variations in OT. Another advantage to obtaining quantitative phase image data is that harmeless light levels are used, and samples do not need to be stained, labeled or marked. The system described in this paper has the ability to track motions of cells, see how cells interact with one another, and follow small motions within cells, tissues and structures.

This paper presents an update on current research [4-9] in developing a Linnik interference microscope specially designed for measurement of living and moving biological samples in epi-illumination. For these examples, objects are viewed in double pass on a reflective surface. The method is extensible to measurement in transmission, or for use with immersion objectives. Here we discuss the current instrument design and modeling tradeoffs as well as methods of image processing to enable extraction of position and OT information.

* email: kcreath@ieee.org

Three-Dimensional and Multidimensional Microscopy: Image Acquisition and Processing XX,
edited by Carol J. Cogswell, Thomas G. Brown, Jose-Angel Conchello, Tony Wilson, Proc. of SPIE Vol. 8589,
85891A · © 2013 SPIE · CCC code: 1605-7422/13/$18 · doi: 10.1117/12.2008751

2. MICROSCOPE DESCRIPTION

Techniques developed for full-field phase-imaging interference microscopes have historically relied upon temporal phase-measurement methods that obtain interferograms sequentially, and therefore require good vibrational damping with static specimens in order to obtain high-quality data [10]. These techniques have been underutilized for biological measurements because they are sensitive to motion and vibration [1-3, 11-14]. The technique presented here incorporates a pixelated phase mask enabling simultaneous capture of all data to determine phase in a fraction of a millisecond.

2.1 Dynamic quantitative phase microscope

The interference microscope used for this work is based upon a Linnik configuration [10, 15]. It is comprised of a Köhler-type illumination system, and a simple imaging system as shown in Fig. 1.

The incoming illumination passes through a polarizing beamsplitter before the microscope objectives creating orthogonal linearly polarized test and reference beams. The relative irradiances of the object and reference beam can be balanced for maximum contrast by adjusting the angle of the polarizer. A quarter-wave plate (QWP) before the camera converts the two polarized beams to right- and left-handed circular polarization to produce interference fringes at the pixelated phase mask. For the measurements in this paper, samples in water or other liquids are placed on a mirror under a cover slip providing a double pass through the object. Sources with wavelengths of 660 nm and 785 nm were used with 20X NA 0.45, or 50X NA 0.8 objectives. The imaging "tube" lens magnification (combination of tube and FOV lenses) varies from 1X to 2.25X.

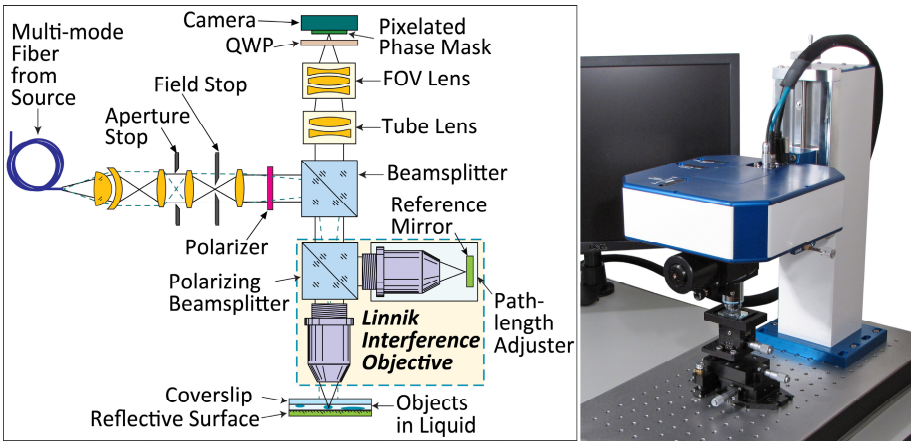

Fig. 1. Optical schematic and photograph of dynamic quantitative phase microscope.

Fig. 1 (right) shows a photograph of an engineering brassboard system. The Linnik objective is seen below the microscope (blue and white box) with a 5-axis translation stage beneath it for adjusting position and tip/tilt of the sample. This compact design enables it to be used on a variety of stands so that it can be interfaced with different types of staging and cell handling systems.

2.2 Phase imaging with a pixelated phase mask

Pixelated micropolarizer arrays were first used for imaging polarimetry [16]. They were adapted for use in phase measurement interferometry in the last decade [17-19]. For phase imaging applications, pixelated phase mask technology enables single frame phase measurement, and permits the use of a wide variety of wavelengths and source bandwidths [20]. All necessary information to determine phase is recorded in a single snapshot. Vibration isolation, phase shifting, or scanning through focus are not needed.

The masks used in this system are comprised of wire-grid polarizers and have been described in references [17-20] (see Fig. 2). The micropolarizers are oriented in the plane of the mask at four different angles θ_i yielding relative phase shifts between right- and left-handed circularly polarized object and reference beams of α_i.

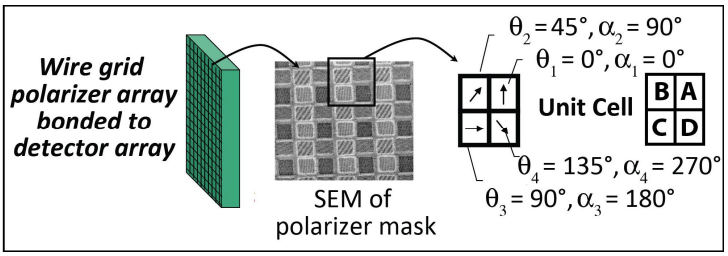

Fig. 2. A pixelated phase mask is bonded to the detector array. It is comprised of a unit cell having 4 different polarization orientations creating 4 different relative phase values.

2.3 Obtaining quantitative phase images

At the phase mask, the reference and test beams have orthogonal circular polarizations (i.e., right-hand circular and left-hand circular). When the two beams are combined, the measured irradiance at each pixel of the camera is given by Eq. (1) [21],

$$I_i(x,y) = \tfrac{1}{2}\{I_O + I_R + 2\sqrt{I_O I_R}\cos[2\Delta\phi(x,y) + \alpha_i]\}, \quad (1)$$

where I_O and I_R are the irradiance of the object and reference beams respectively, α_i is the phase shift between the object and reference beams induced by the micropolarizer at angles θ_i with respect to the *x, y* plane, and $2\Delta\phi(x,y)$is the total phase difference between the object and reference beams for the double pass through the object reflecting off the mirror. When this equation is applied to each of the 4 pixel types in the unit cell (Fig. 2) phase differences of 0°, 90°, 180°, and 270° are encoded into interferograms that can be written as Eqs. (2)-(5):

$$A(x,y) = \tfrac{1}{2}\{I_O + I_R + 2\sqrt{I_O I_R}\cos[2\Delta\phi(x,y)]\}, \quad (2)$$

$$B(x,y) = \tfrac{1}{2}\left\{I_O + I_R + 2\sqrt{I_O I_R}\cos\left[2\Delta\phi(x,y) + \tfrac{\pi}{2}\right]\right\}, \quad (3)$$

$$C(x,y) = \tfrac{1}{2}\{I_O + I_R + 2\sqrt{I_O I_R}\cos[2\Delta\phi(x,y) + \pi]\}, \quad (4)$$

and

$$D(x,y) = \tfrac{1}{2}\left\{I_O + I_R + 2\sqrt{I_O I_R}\cos\left[2\Delta\phi(x,y) + \tfrac{3\pi}{2}\right]\right\}. \quad (5)$$

From a single image, four simultaneous full-field interferograms are synthesized by combining pixels of each phase type (A, B, C and D). These four interferograms can be processed by a variety of algorithms that are well-known for calculating image phase [22, 23]. Using the common four-frame phase algorithm, the double-pass quantitative phase variation is written in Eq. (6) as

$$2\Delta\phi(x,y) = ATAN2\left[\frac{D(x,y) - B(x,y)}{A(x,y) - C(x,y)}\right], \quad (6)$$

where *ATAN*2 is the 2π arctangent function. This produces a modulo 2π (wrapped) phase map which then needs to be unwrapped using standard techniques [24, 25]. These phase image calculations with unwrapping can be done in real-time [26].

2.4 Determining OPD and optical thickness

Each interference fringe in reflection corresponds to one-half wave of optical path difference (OPD) given by

$$OPD(x,y) = \frac{\Delta\phi(x,y)}{4\pi}. \tag{7}$$

Typically, the raw units of OPD are in terms of wavelengths of the source light (waves). When measuring transparent objects such as glass, optical coatings and liquid media, optical metrologists often refer to these OPD variations as optical thickness (OT). Whereas OPD is typically presented in units of waves (or wavelengths), but can also have the units of length, OT has units of length. We are defining OT as

$$OT(x,y) = \lambda \cdot OPD(x,y) = \lambda \cdot \Delta\phi(x,y)/4\pi, \tag{8}$$

and

$$OT(x,y) = OPL_O(x,y) - OPL_R(x,y), \tag{9}$$

where $OPL_O(x,y)$ and $OPL_R(x,y)$ are the integrated optical path lengths, $OPL = \int_0^{path} n\,dz$, for the object and reference beams as defined in Ref. [27]. For quantitative phase imaging OPD and OT can be used interchangeably.

OT and OPD values are **not** the actual physical thickness of a transparent object. They both incorporate the integrated OPL where the refractive index and physical thicknesses are coupled. These two quantities cannot be separated without *a priori* information about one or the other.

When transparent biological objects are surrounded by liquids such as water and placed between a mirror and a cover slip, thicker areas of the object or areas with higher refractive indices will yield larger OT values as shown in the profile on the bottom of Fig. 3.

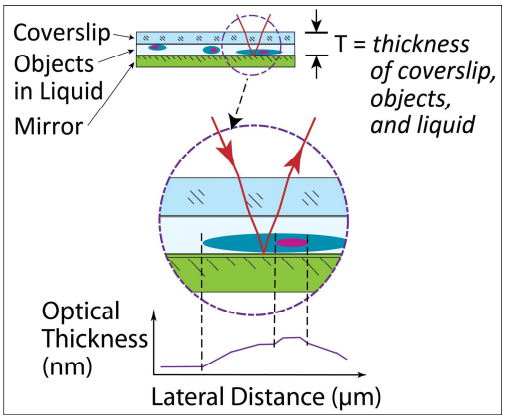

Fig. 3. Optical path length through test sample includes the coverslip, liquid and objects. Graph (bottom) shows an OT profile for the section within the circled area.

For the examples shown in this paper, we are presenting the measured OT or OPD. We have not assumed any refractive index or cell thickness values. Because of this, the vertical scales appear to be compressed. To illustrate this concept, if an object has a physical thickness of 10µm and has a refractive index variation of 0.05 greater than the liquid surrounding it (e.g. an object index of 1.38 in water of index 1.33), then the OT will have a value of 500 nm peak to valley relative to the background, while the OPD would be 0.75 waves peak to valley for a wavelength of 660 nm.

As an example, a quantitative phase image of some MCF715 breast cancer cells is shown in Fig. 4. Cells grown on a coverslip were placed upsidedown on a highly reflective mirror with cell nutritional media filling in between the mirror and coverslip. These images were taken at 20X with a 1.67X tube lens, a 660 nm source and 2 ms exposures. Note that the intercellular matrix and newly forming cells around the edges of the matrix are clearly visible and easily resolved as are organelles and nuclei within the cells. The lateral sampling in the image for this

exposure is 0.53 μm for each 4-pixel 2x2 cell in the pixelated phase mask. The optical resolution at NA=0.45 is 0.9 μm (0.61 λ/NA) yielding a slightly oversampled image. These data have had the background shape removed which is described later in this paper.

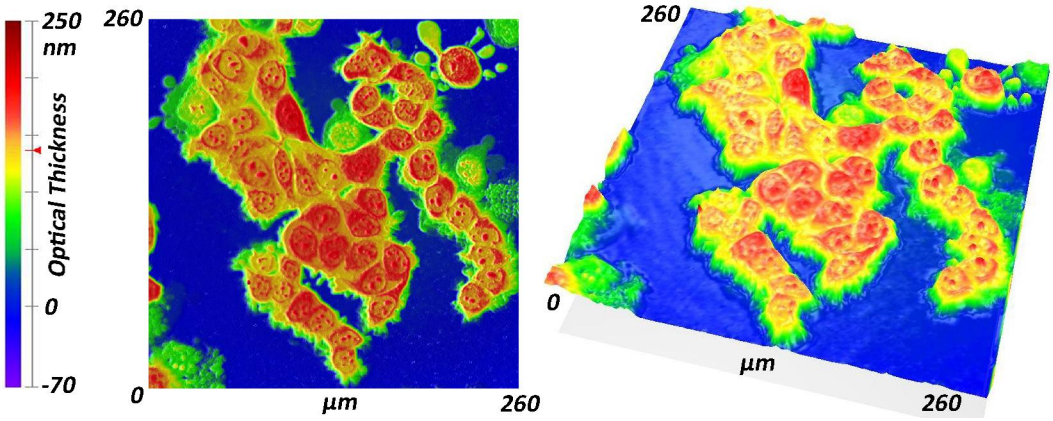

Fig. 4. Quantitative phase image of breast cancer cells grown on a coverslip taken with a 20X Linnik objective at 660 nm. The optical thickness scale is pseudo-colored to show the relative index of refraction variations of different cellular components.

3. OPTICAL PERFORMANCE

3.1 Optical performance and measurement sensitivity

Because there is always a tradeoff between getting the maximum FOV and the best optical resolution, the system design was modified to have two different fields of view (FOV) using a flip-in FOV lens in the imaging arm. This does not change the optical resolution of the microscope, but enables choosing between using a large FOV, or maximizing resolution by changing the total system magnification by a factor of 2.25X. With 20X objectives, this yields 20X and 45X. The system utilizes a camera with a pixel pitch of 7.4 μm and sensing area of 9.2 x 8.88 mm yielding a 20X FOV of 460 x 440 μm and 204 x 197 μm at 45X.

The phase sensitivity and instrument noise were determined by taking two consecutive phase measurements without an object present. The rms of the point-by-point difference between the two measurements indicates the measurement repeatability and provides a standard measure of the instrument noise level [28]. For this instrument, the rms repeatability for single measurements is ~1.0 nm. This means that the spatial phase sensitivity between pixels in the same measurement is ~1.0 nm, and the temporal phase sensitivity over short periods of time will also be ~1.0 nm. The performance over longer periods of time depends upon the thermal and mechanical stability of the environment. Other details on optical performance have been noted in previous papers [4-9].

3.2 Effects of incoherent imaging

Obtaining high quality interference fringes with these types of sources requires tight tolerances on the optical system to equalize path lengths [29, 30]. A major requirement for this type of microscope is that the spatial and temporal coherence functions need to overlap one another for high quality interference fringes [31, 32]. Dispersion induced by the coverslip, transparent object, and liquid, will shift the spatial coherence function relative to the temporal coherence function and can reduce fringe modulation. One way of dealing with this is to put an equivalent amount of glass and liquid in the reference arm as in the test arm to equalize optical path lengths [33], or change the illumination system to account for it [31-33].

Another way to get around this limitation is to tailor the temporal and spatial coherence functions to accommodate unmatched dispersive media in both arms and still have the positive effects of low coherence [31, 32]. This is done by designing the source so that the temporal coherence length is long enough to account for the path length differences generated by the dispersive media (the cover slip and liquid), while reducing the spatial coherence to localize the interference fringes in space, so that spurious reflections and coherent noise are not present.

To illustrate this we have begun modeling the microscope system using non-sequential ray tracing. This model depicts the essential parts of a Michelson interferometer and does not include all the components in the current microscope. The x-scale of the plot is relative motion between the reference and test beams. Fig. 5 shows results of modeling the temporal coherence for sources with bandwidths of 1.5nm and 35nm. The 35nm bandwidth source localizes the fringes in a small area, whereas the 1.5nm bandwidth source has a broader temporal coherence. Adding dispersive media in the test path causes there to be a shift of the fringe modulation peak that needs to be compensated by moving the reference mirror. If the source is extended, then the temporal coherence function must be broad enough to have decent fringe modulation at both reference mirror positions. We will show further modeling results in a future paper.

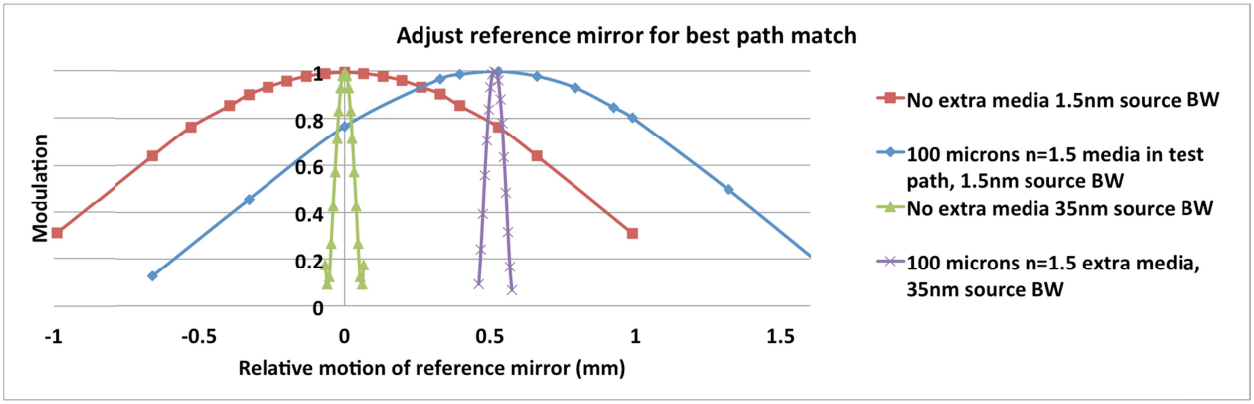

Fig. 5. Modeling results showing effects of temporal coherence in an interferometer for two different source bandwidths, with and without extra dispersive media in the test arm of the interferometer. Note that the narrower bandwidth source has a wider temporal coherence range and that the reference mirror can be moved to maximize fringe modulation to compensate for the extra media. This model does not include the effects of spatial coherence.

In our design we reduced spatial coherence to ~25-35 µm by utilzing diode laser sources having temporal coherence lengths of 250-300 µm (spectral bandwidths of ~1.5 nm) focused onto a rotating diffuser [15] and then coupled into an NA 0.2 multi-mode optical fiber with a 1000 µm core. The laser has sufficient temporal coherence over path length differences that take into account the cover glass, while the spatial size of the source given by the multi-mode optical fiber limits the spatial coherence.

4. REMOVAL OF BACKGROUND SURFACE STRUCTURE

Ultimately, the objective of quantitative phase imaging is to follow motion or to find relative changes over time within a sample. In order to do this, we need to insure that we are isolating the object relative to the background so that the OT corresponds to the object of interest and not some variation in the thickness of the coverslip, the shape of the reflective mirror under the sample, the thickness of the liquid layer, or alignment of the sample relative to the microscope. Normally when aligning an object for a measurement, we want to level the background as much as possible. Slight variations in the coverslip, mirror or liquid layer will not be eliminated this way and it is not always possible to remove the background shape by simply aligning the sample. Systematic errors in the optical system can be removed by well-known techniques of generating a reference surface containing errors within the optical system and subtracting that from data [28]. But this will not deal with variations within the object or its alignment. To do this, we need to differentiate between the object and the background.

4.1 Manual background leveling with user defined background areas

To illustrate this, Fig. 6 shows cell cultures of the MCF715 human breast cancer line grown in cell media on coverslips. To image these cells, the coverslips are placed upside down on a highly reflective mirror with their growth media filling in between the mirror and coverslip. These images were taken at 20X with a 1.67X tube lens, a 660 nm source and 2 ms exposures. Fig. 6(a) shows an interferogram with 4 fringes of tilt in the background. The fringes are slightly curved showing that there is also some curvature present due to the mirror or

misalignment. The unwrapped phase is shown in Fig. 6(b) while the raw OT data are shown in Fig. 6(c). Typically in interferometer systems, tilt will be removed by a least squares fit of a plane to the entire dataset and then subtracting that plane from the data. When this is done on a relatively featureless scene, it works quite well, but when there are a number of objects within the field of view as in this example, it does not level the data very well relative to the background as seen in Fig. 6(d). When the background areas to fit the plane to are defined by the rectangles in Fig. 6(e), the resulting data are then independent of the background tilt as seen in Fig. 6(e). This manual technique works, but is tedious and will not work if the areas defined are encroached upon by moving objects as a time series is processed. It is also possible to filter the OT histogram to isolate the object from the background [9], but this only works for simple objects.

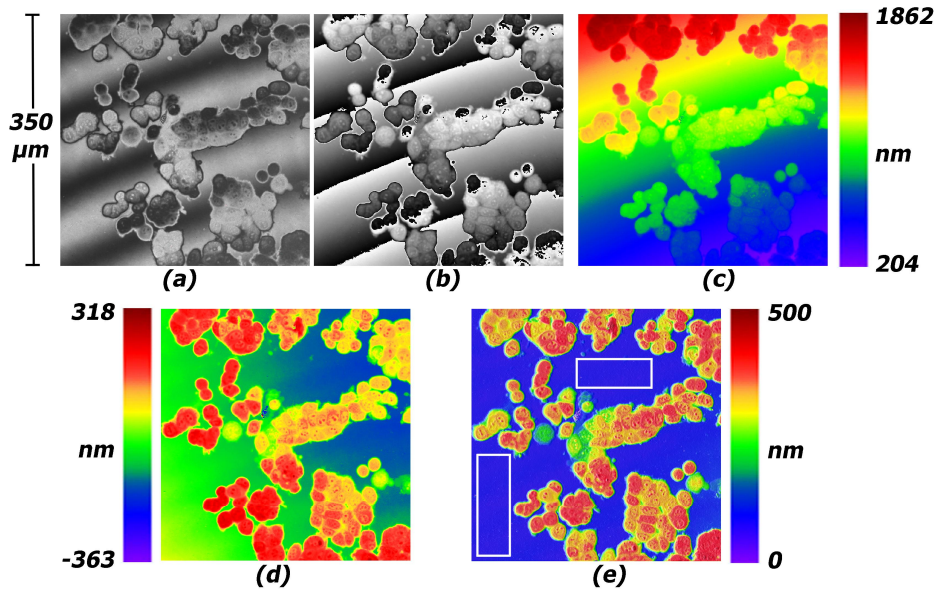

Fig. 6. Human breast cancer cells taken with 20X magnification at 660 nm. (a) Interference pattern showing 4 fringes of tilt. (b) Modulo 2π wrapped phase. (c) Unwrapped optical thickness in nm from phase. (d) Best-fit plane removed. (e) OT with manual background removal using the areas defined by the white rectangles.

4.2 Automated background leveling using gradient thresholding

A more robust background-leveling algorithm has been developed that operates very well on scenes that have varied sizes of phase objects against a background. The algorithm is based on techniques that utilize thresholding with respect to gradients of the data [34, 35]. By considering the gradient magnitudes of the phase, [36]

$$PGM = \sqrt{\left(\frac{\partial \phi}{\partial x}\right)^2 + \left(\frac{\partial \phi}{\partial y}\right)^2}, \tag{10}$$

rather than the phase values, regions where the phase is slowly varying can be automatically identified. The general assumption is made that the slope magnitude value that has the maximum occurrence is assumed to be associated with the background. This assumption is generally valid for images obtained by this microscope. The background leveling routine consists of the following steps:

1. Calculate gradient magnitudes as defined in Eq. (10).
2. Iteratively threshold data outside a given range centered about the maximum occurrence of gradient magnitude such that enough pixels have been masked.
3. Grow the mask to incorporate nearest neighbors of masked pixels.
4. Apply mask to phase data and calculate low-order Zernike background surface from non-masked pixels.
5. Remove background surface from original phase data.

This technique is illustrated using an example where the object dominates the field of view. The measured optical OT data of the tail end of a rotifer are shown in Fig. 7(a). The gradient magnitudes shown in Fig. 7(e). Areas where the gradient magnitude is above a set relative threshold are masked out of the data set. For subsequent iterations, the gradient magnitudes of the remaining pixels are calculated, and pixels above a set relative threshold are further masked. This process is repeated until either the number of pixels masked reaches a set limit or until the values of the gradient magnitudes left in the data set are below a set relative threshold. Fig. 7(f)-(i) show this process through 4 iterations. The final binary mask is shown in Fig. 7(b). Note that most of the pixels in the object have been masked out (white pixels), and variations in the background are also masked out. This type of algorithm is compatible with implementation within GPU processors to provide real-time processing.

Once this generated mask has been applied to the OT data, the remaining data are fit with a Zernike surface using a least squares fit. Because the predominant background shape is a tilted plane, the fit is to the first 3 Zernike terms including piston (mean value) and tilt in the x and y directions (see Ref [37] for a definition of these terms). The planar Zernike surface representing the background shape that needs removing is shown in Fig. 7(c). This surface is then subtracted from the original data (Fig. 7(a)) and shown in Fig. 7(d). At this point quantitative OT data can be extracted from the object independent of the background. Remember that this assumes that the overall thickness of the coverslip, objects, and media are constant, and that there are not multiple objects stacked on top of one another. This processing enables relative changes from frame to frame in a time series to be quantified.

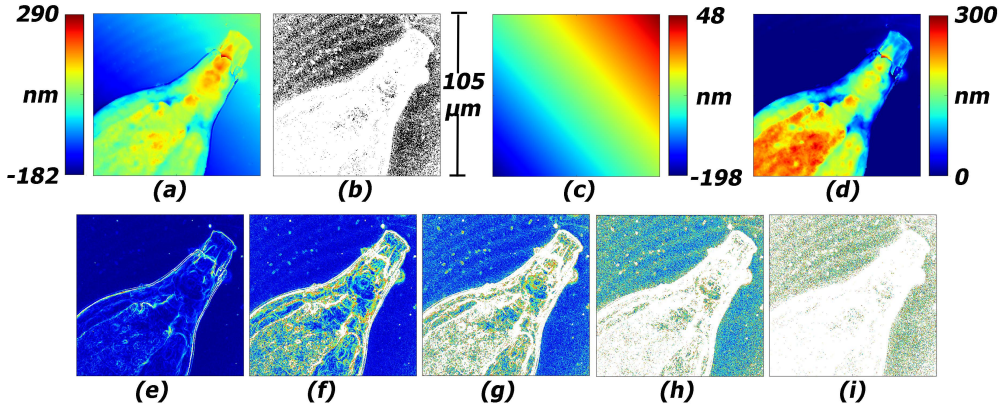

Fig. 7. Rotifer tail imaged with 50X at 660 nm. (a) Optical thickness calculated from raw phase. (b) Final binary mask corresponding to background area for fitting Zernike surface. (c) Best fit plane (synthetic 3-term Zernike surface) corresponding to background surface to remove. (d) OT after automatic background removal. (e) Gradient magnitudes from (a). (f)-(i) Iterations 1 to 4 to determine area to mask.

5. SAMPLE MEASUREMENTS

5.1 Types of images obtainable

The pixelated phase mask sensor enables a number of different types of images to be obtained simultaneously as illustrated in images of a protozoa in Fig. 8. These were taken at 50X with a 660 nm source. When the values of all 4 types of pixels from Fig. 2 are averaged, a brightfield image is obtained (Fig. 8(a)). When values from one type of pixel are displayed, an interferogram or phase-contrast image is obtained (Fig. 8(b)). Simulated dark field (SDF) images with illumination coming from an annulus highlighting the edges are generated by calculating the phase gradient magnitudes using Eq. (10) (Fig. 8(c)) [36]. Simulated DIC (differential interference contrast) images are obtained by calculating the gradient of the phase in the x or y direction (Fig. 8(d)).

Combining all 4 pixels using Eqs. (2)-(9) produces a phase image which then is scaled relative to the wavelength providing a pseudo-colored OT map (Fig. 8(e)). Fig. 8(f) shows a composite image enhancing the structural variations within the measured sample. Fig. 8(f) shows an enhanced OT plot comprised of a composite of

measurement channels that highlights OT topography. A 3D topographic plot of OT is shown Fig. 8(h). The OT range of this sample is about 375 nm maximum (red) to minimum (blue)(peak-to-valley or P-V). This is not the physical thickness of the protozoa. Because these are relative and not absolute measurements, we have arbitrarily set the minimum value to zero. Note that internal structures are readily visible.

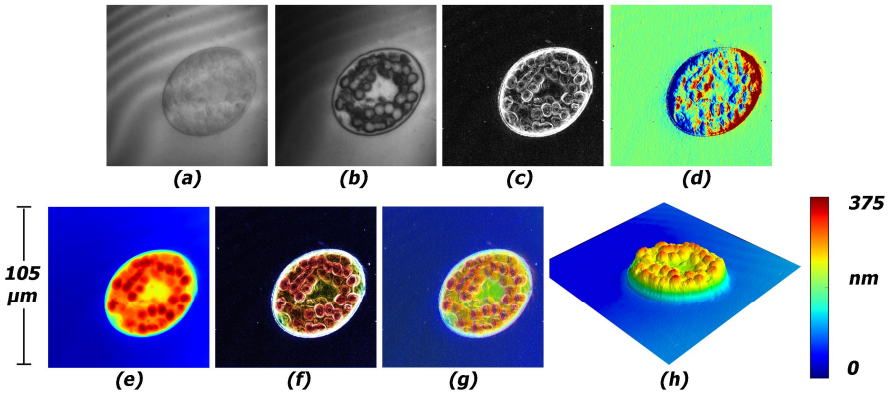

Fig. 8. Images of a protozoa determined from pixelated phase data. (a) Brightfield (irradiance/intensity). (b) Phase contrast (interference – a single interferogram). (c) SDF (phase gradient magnitudes). (d) Simulated DIC (x gradient). (e) Pseudo-colored OT (from phase). (f)-(g) Enhanced OT images. (h) 3D topographic OT plot. Plots in bottom row have same color scale. Data for all these image types is obtained from a single snapshot. See Video 1. http://dx.doi.org/10.1117/12.2008751.1

Another example (shown in Fig. 9) is a cropped subset of the data in Fig. 6. The dominating background shape is more complicated with a curved background requiring higher-order Zernike terms to fit a background surface (see curved fringes in Fig. 6). When larger-term Zernike fits are necessary, the need to ignore objects becomes more critical because the spherical shape of cells can confuse a simple background subtraction technique if those objects are not ignored with a mask. The optical thickness data with the background surface removed are shown in Fig. 9(a). The SDF image is shown in Fig. 9(b) while the simulated DIC image is shown in Fig. 9(c). An enhanced OT composite image highlighting topography is shown in Fig. 9(d).

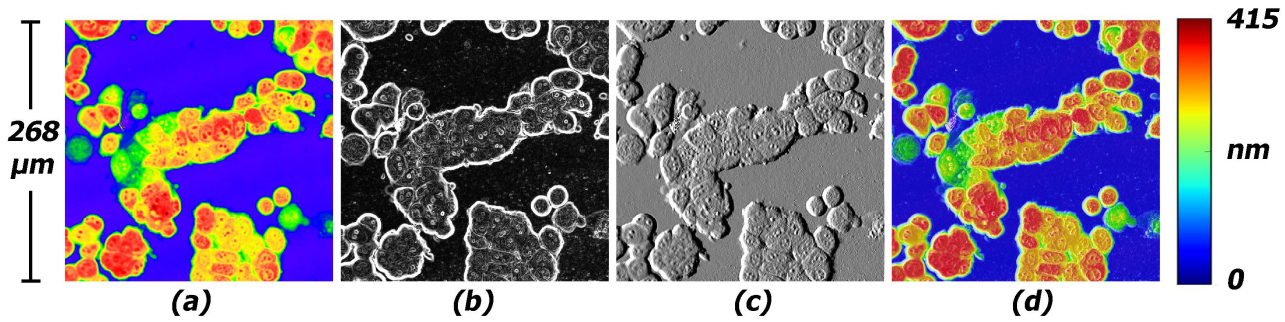

Fig. 9. Images of breast cancer cell derived from pixelated phase data with background removed. (a) Pseudo-colored OT (from phase). (b) SDF (phase gradient magnitudes). (c) Simulated DIC (x gradient). (d) Enhanced OT.

5.2 Dynamic measurement of moving biological objects

Dynamic measurements are made using short exposures on the order of 0.5-1ms with user specified time delays between frames of data ranging from no delay to several hours. The current maximum achievable acquisition rate is 25 frames per second (fps) in full frame mode. The data are processed to obtain unwrapped phase, and then movies can be compiled from the time series of images. An example of capturing dynamic motion is shown in Video 1 for the protozoa in Fig. 8. This movie shows the same motion sequence for each of the different types of images. Note that the motion of the cilia and organelles inside the protozoa are visible.

Examples of the motion of cilia in a large paramecium are shown below in Fig. 10 and Video 2. This series of images was taken at 15 fps (time delays of ~0.065 between exposures). These images have a magnification of 50X with a 660 nm source. Note that the cilia and their motion from frame to frame are highly visible as are small motions of the body and organelles within the body.

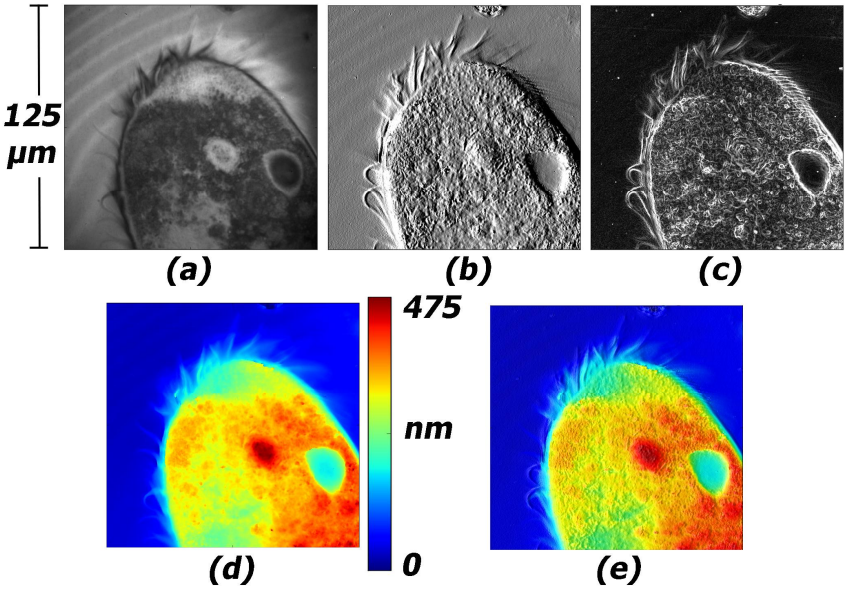

Fig. 10. Sample images from a time series movie of a large paramecium taken with 50X magnification at 660 nm. (a) Phase contrast (interference). (b) Simulated DIC (x gradient). (c) SDF (Phase gradient magnitudes). (d) OT (from phase). (e) Enhanced OT. Note motion of cilia in Video 2. http://dx.doi.org/doi.number.goes.here

6. DISCUSSION AND CONCLUSIONS

This paper has described recent research and development of a dynamic quantitative phase imaging microscope and shown a number of examples of dynamic phase measurements of living biological organisms. All data required to determine phase and optical thickness are gathered in a single snapshot utilizing a pixelated phase mask, so no scanning is necessary. Short exposure times freeze motion instantaneously. Data from brightfield imaging, phase contrast (interference image), as well as simulated dark field (phase gradient magnitude) and simulated DIC images (phase gradient), are also obtained simultaneously along with phase and optical thickness.

An automated background-leveling routine has been applied to a wide range of biological samples. By thresholding the gradient magnitudes of the optical thickness data, objects can be successfully masked, leaving only pixels associated with the background that can then be characterized with a low-order Zernike surface. This method successfully removes background shape without the need for user input and is easily scalable to process large numbers of data frames of moving objects.

These methods can be extended to higher magnifications, immersion objectives, higher numerical apertures, a large range of wavelengths, and to measure cells in transmission. Harmless light levels offer a non-destructive means of observing and quantifying biological behavior and dynamic variations over time. The ability to dynamically measure biological organisms in real time opens up many different types of applications ranging from flow cytometry to tissue dynamics, morphological and volumetric studies along with mechanistic studies, process monitoring, quantification of cellular motion, monitoring and tracking cellular damage under known perturbations, tracking cell migration, nerve and muscle transmission, histology and photodynamic therapy. This measurement model can be further modified to include simultaneous fluorescence measurements to more specifically track particular mechanisms.

7. ACKNOWLEDGEMENTS

The authors wish to acknowledge Tim Horner, Mark McKune, Richard Robinson, Neal Brock, and Dr. James Millerd from 4D Technology Corp. for their assistance in this project, Dr. Andy Rouse, Dr. Ron Lynch, Craig Weber and Jordan Barton from The University of Arizona for their assistance in obtaining cell measurements, and Howard Letovsky. This work partially supported by NIH/NCRR 1R43RR028170-01, 2R44RR028170-02, and NIH/NIGMS 8 R44 GM103406-03.

8. REFERENCES

[1] Popescu, G., "Quantitative phase imaging of nanoscale cell structure and dynamics," in [Methods in Nano Cell Biology, Volume 90], Jena, B. P., ed., Elsevier, San Diego, 87-115, (2008).
[2] Popescu, G., [Quantitative Phase Imaging of Cells and Tissues], Mc-Graw Hill, New York, (2011).
[3] Reed, J., Frank, M., Troke, J. J., Schmit, J., Han, S., Teitell, M. A., and Gimzewski, J. K., "High throughput cell nanomechanics with mechanical imaging interferometry," Nanotechnology 19(23), 235101 (2008).
[4] Creath, K., "Dynamic quantitative phase images of pond life, insect wings, and in vitro cell cultures," Proc. SPIE 7782, 77820B.77801-77813 (2010).
[5] Creath, K., "Dynamic phase imaging utilizing a 4-dimensional microscope system," Proc. SPIE 7904, 79040O (2011).
[6] Creath, K., "Dynamic phase imaging for in vitro process monitoring and cell tracking," Proc. of the 33rd Ann. Int'l Conf. of the IEEE EMBS, Boston, Ma, August 29-September 3, 2011 33, 5977-5980 (2011).
[7] Creath, K., and Goldstein, G., "Dynamic phase imaging and processing of moving biological organisms," Proc. SPIE 8227, 82270M (2012).
[8] Creath, K., and Goldstein, G., "Dynamic quantitatione phase imaging for biological objects using a pixelated phase mask," Biomedical Optics Express 3(11), 2866-2880 (2012).
[9] Goldstein, G., and Creath, K., "Dynamic four-dimensional microscope system with automated background leveling," Proc. SPIE 8493, 84930N (2012).
[10] Schmit, J., Creath, K., and Wyant, J. C., "Ch. 15. Surface profilers, multiple wavelength, and white light interferometry," in [Optical shop testing; 3rd Edition], Malacara, D., ed., Wiley-Interscience, Hoboken, N.J., 667-755, (2007).
[11] Dunn, G. A., and Zicha, D., "Phase-shifting interference microscopy applied to the analysis of cell behaviour," Symp. Soc. Exp. Bio. 47, 91-106 (1993).
[12] Tychinsky, V. P., Kretushev, A. V., Klemyashov, I. V., Vyshenskaya, T. V., Filippova, N. A., Raikhlin, N. T., and Shtil, A. A., "Quantitative real-time analysis of nucleolar stress by coherent phase microscopy," J. Biomed. Opt. 13(6), 064032 (2008).
[13] Yang, C., Wax, A., Hahn, M. S., Badizadegan, K., Dasari, R. R., and Feld, M. S., "Phase-referenced interferometer with subwavelength and subhertz sensitivity applied to the study of cell membrane dynamics," Opt. Lett. 26(16), 1271-1273 (2001).
[14] Yu, L. F., Mohanty, S., Liu, G. J., Genc, S., Chen, Z. P., and Berns, M. W., "Quantitative phase evaluation of dynamic changes on cell membrane during laser microsurgery," J. Biomed. Opt. 13(5), 050508 (2008).
[15] Gale, D. M., Pether, M. I., and Dainty, J. C., "Linnik microscope imaging of integrated circuit structures," Appl. Opt. 35(1), 131-148 (1996).
[16] Nordin, G. P., Meier, J. T., Deguzman, P. C., and Jones, M. W., "Micropolarizer array for infrared imaging polarimetry," J. Opt. Soc. Am. A 16(5), 1168-1174 (1999).
[17] Brock, N. J., Millerd, J. E., Wyant, J. C., and Hayes, J. B., "Pixelated phase-mask interferometer," USPTO, ed., 4D Technology Corporation, United States, (2007).
[18] Kimbrough, B. T., "Pixelated mask spatial carrier phase shifting interferometry algorithms and associated errors," Appl. Opt. 45(19), 4554-4562 (2006).
[19] Novak, M., Millerd, J., Brock, N., North-Morris, M., Hayes, J., and Wyant, J., "Analysis of a micropolarizer array-based simultaneous phase-shifting interferometer," Appl. Opt. 44(32), 6861-6868 (2005).
[20] Moxtek, "Pixelated polarizers," http://www.moxtek.com/optics-products/pixelated-polarizers.html (2010).

[21] Kothiyal, M. P., and Delisle, C., "Shearing interferometer for phase-shifiting interferometry with polarization phase-shifter," Appl. Opt. 24(24), 4439-4442 (1985).
[22] Creath, K., "Phase-measurement interferometry techniques," in [Progress in Optics], Wolf, E., ed., Elsevier Science Publishers, Amsterdam, 349-393, (1988).
[23] Malacara, D., ServÌn, M., and Malacara, Z., [Interferogram analysis for optical testing], Taylor & Francis, Boca Raton, FL, (2005).
[24] Robinson, D. W., "Phase unwrapping methods," in [Interferogram Analysis], Robinson, D. W., and Reid, G. T., eds., IOP Publishing, Bristol, 194-229, (1993).
[25] Ghiglia, D. C., and Pritt, M. D., [Two-Dimensional Phase Unwrapping: Theory, Algorithms and Software], Wiley-Interscience, New York, (1998).
[26] Hwang, W.-J., Chang, S.-C., and Cheng, C.-J., "Efficient phase unwrapping architecture for digital holographic microscopy," Sensors 11, 9160-9181 (2011).
[27] Born, M., and Wolf, E., [Optics, 7th Ed.], Cambridge Univ. Press, Cambridge, (1999).
[28] Creath, K., and Wyant, J. C., "Absolute measurement of surface roughness," Appl. Opt. 29(26), 3823-3827 (1990).
[29] Farr, K. B., and George, N., "Beamsplitter cube for white light interferometry," Opt. Eng. 31(10), 2191-2196 (1992).
[30] Pfortner, A., and Schwider, J., "Dispersion error in white-light Linnik interferometers and its implications for evaluation procedures," Appl. Opt. 40(34), 6223-6228 (2001).
[31] Abdulhalim, I., "Competence between spatial and temporal coherence in full field optical coherence tomography and intererence microscopy," J Opt A: Pure Appl. Opt. 8, 952-958 (2006).
[32] Ryabukho, V., and Lyakin, D., "Longitudinal pure spatial coherence of a light field with wide frequency and angular spectra," Opt. Lett. 30(3), 224-226 (2005).
[33] Han, S., "Interferometric testing through transmissive media," Proc. SPIE 6293, 629305 (2006).
[34] Weszka, J. S., "A survey of threshold selection techniques," Comp. Graph. Imag. Proc. 7(2), 259-265 (1978).
[35] Yanowitz, S. D., and Bruckstein, A. M., "A new method for image segmentation," Comp. Vis. Graph. Imag. Proc. 46(1), 82-95 (1989).
[36] Kekre, H., Thepade, S., Mikherkee, P., Kakaiya, M., Wadhwa, S., and Singh, S., "Image retrieval with shape features extracted using gradient operators and slope magnitude technique with BTC," Int'l J. Comp. Appl. 6(8), 28-33 (2010).
[37] Wyant, J. C., and Creath, K., "Basic wavefront aberration theory for optical metrology," in [Applied Optics and Optical Engineering, Volume XI], Shannon, R. R., and Wyant, J. C., eds., Acad. Press, San Diego, 1-53, (1992).